Mountain Waves Produced by a Stratified Boundary Layer Flow. Part I: Hydrostatic Case

François Lott, Bruno Deremble, Clément Soufflet

▶ **To cite this version:**

François Lott, Bruno Deremble, Clément Soufflet. Mountain Waves Produced by a Stratified Boundary Layer Flow. Part I: Hydrostatic Case. Journal of the Atmospheric Sciences, 2020, 77 (5), pp.1683-1697. 10.1175/JAS-D-19-0257.1 . hal-02998000

HAL Id: hal-02998000

https://hal.sorbonne-universite.fr/hal-02998000

Submitted on 10 Nov 2020

HAL is a multi-disciplinary open access archive for the deposit and dissemination of scientific research documents, whether they are published or not. The documents may come from teaching and research institutions in France or abroad, or from public or private research centers.

L'archive ouverte pluridisciplinaire **HAL**, est destinée au dépôt et à la diffusion de documents scientifiques de niveau recherche, publiés ou non, émanant des établissements d'enseignement et de recherche français ou étrangers, des laboratoires publics ou privés.

Journal of the Atmospheric Sciences: Revised Version (11) of January 30^{th}, 2020, accepted February 27^{th}, 2020

Mountain waves produced by a stratified boundary layer flow. Part I: Hydrostatic case.

François Lott[1], Bruno Deremble, and Clément Soufflet

Laboratoire de Météorologie Dynamique, Ecole Normale Supérieure, PSL Research Institute, 24 rue Lhomond, 75231 Paris France

Abstract

An hydrostatic theory for mountain waves with a boundary layer of constant eddy viscosity is presented. It predicts that dissipation impacts the dynamics over an inner layer which depth is controlled by the inner layer scale δ of viscous critical level theory. The theory applies when the mountain height is smaller or near δ and is validated with a fully nonlinear model. In this case the pressure drag and the waves Reynolds stress can be predicted by inviscid theory, if one takes for the incident wind its value around the inner layer scale. In contrast with the inviscid theory and for small mountains the wave drag is compensated by an acceleration of the flow in the inner layer rather than of the solid earth. Still for small mountains and when stability increases, the emitted waves have smaller vertical scale and are more dissipated when traveling through the inner layer: a fraction of the wave drag is deposited around the top of the inner layer before reaching the outer regions. When the mountain height becomes comparable to the inner layer scale non-separated upstream blocking and downslope winds develop. Theory and model show that (i) the downslope winds penetrate well into the inner layer, (ii) upstream blocking and downslope winds are favored when the static stability is strong and (iii) are not associated with upper level wave breaking.

[1]Corresponding author: flott@lmd.ens.fr

1. Introduction

The impact of small to medium scale mountains on the atmospheric dynamics has been intensively studied over the last 50 years by two quite distinct communities. One community is studying how mountains modify the turbulent boundary layer (Jackson and Hunt, 1975), an issue that is central in the context of wind resource modeling (Ayotte, 2008) or dune formation (Charru et al., 2012). The associated theories form the basis of subgrid scale orography parameterizations, where the enhancement of turbulence caused by mountains is modeled by increasing the terrain roughness length (Wood and Mason, 1993). Wood et al. (2001) used fully nonlinear simulations to extend the theory and improve the estimate of the depth over which the mountain drag is deposited. These parameterizations are used for mountains with horizontal scales smaller than 5000 m (Beljaars et al., 2004). At these scales one can expect that the horizontal scale of the mountains, L, is such that the advective time scale, L/u_0 is smaller than the inverse of the buoyancy frequency N^{-1}. This ensures that the flow behaves according to neutral flow dynamics.

The second community is more focused on mountain dynamical meteorology. It studies the onset of downslope winds, foehn, and trapped waves using theories and models where internal gravity waves control the dynamics, and where the boundary layer is often neglected. The relevance of the approach is illustrated by Sheridan et al. (2017) where a near linear mountain wave model permits to interpret wind perturbations due to mountain wave events over the UK. The associated theory is extremely vast in itself (Durran, 1990). Among other things, this theory has been used to predict realistic partitions between upper level and lower level wave drag and orographic blocking, which are concepts that are used in parameterizations of subgrid scale orography with horizontal scales $L > 5000$ m (Lott and Miller, 1997). Note that this type of parameterization is still used in atmospheric models, and even in the models with horizontal resolution that resolve these scales (Sandu et al., 2015; Pithan et al., 2016). In fact, it is not so clear whether there is a critical mountain size ($L = 5000$ m) below which the flow would only impact the boundary layer and above which the flow would only impact the waves. We actually believe that this criteria is quite adhoc and should depend on the nature of the flow.

Because boundary layer dynamics is highly controlled by the inviscid dynamics aloft, and because in mountain meteorology the wave forcing is embedded into the boundary layer, it soon appeared that the two communities should make some effort to integrate results from the other community. It is in this context that Hunt et al. (1988) and Belcher and Wood (1996) included stratification and gravity waves in boundary layer theories over mountain. Belcher and Wood (1996) showed that when the Froude number $F = u_0/NL$ is smaller than 1, the mountain drag is due to mountain gravity waves (rather than boundary layer effect) and is well predicted by linear gravity mountain wave theory. This result actually depends on the height at which one chooses

the reference velocity u_0 and reference Brunt Vaisala frequency N. As we shall see, in the absence of background wind curvature, the relevant altitude to compute these quantities is that of the inner layer, which is the altitude where disturbance advection by the background wind is balanced by dissipation. Still in this context but in the mountain meteorology community, studies using numerical model show that the boundary layer drag reduces downslope windstorms and mountain waves (Richard et al., 1989; Olafsson and Bougeault, 1997). More recent observations show that the atmospheric boundary layer can absorb downward propagating waves and weaken trapped lee waves (Smith et al., 2002; Jiang et al., 2006). These last results have motivated a series of theoretical studies on the interaction between the boundary layer and mountain waves. All so far use crude parameterizations of the boundary layer: Smith et al. (2006) uses a bulk boundary layer model, Lott (2007) usesd constant eddy viscosity, and Lott (2016) uses linear drags (Newtownian cooling and Rayleigh drag).

Despite these simplifications, these studies reproduce the increase in trapped waves absorption when stability increases, insisting on cases where the incident wind is weak near the ground. This near surface critical level situation, a situation that was little studied because it poses fundamental problems in the inviscid mountain wave theory, was nevertheless found to produce interesting dynamics. Near surface critical level favors downslope windstorms and Foehn (Lott, 2016; Damiens et al., 2018) and permits to establish a bridge between trapped lee waves and Kelvin-Helmholtz instabilities (Lott, 2016; Soufflet et al., 2019). Interestingly, the critical level mechanism that is a priori a dissipative mechanism turned out to be extremely active dynamically.

To summarize, there are two descriptions of the interaction between boundary layers and mountain waves: on the one hand boundary layer studies tell that the pressure drag is controlled by the mountain wave dynamics outside of the boundary layer, but imposes very simplified dynamics outside of it (Belcher and Wood, 1996). And on the other hand, "mountain wave" studies that give great attention to the potential impact of a boundary layer on mountain waves but that use very simplified boundary layer representation (Smith et al., 2006). We actually believe that there is still room to develop a theory where the boundary layer and the mountain wave field fully interact in a comprehensive way. We see at least three reasons for this. The first is that in mountain wave theory, the gravity wave (GW) field is controlled by the low level flow amplitude, and it is not obvious to tell at which (or over which) altitude it should be measured in the absence of strong wind curvatures. Second, we know that the inviscid dynamics potentially produces downslope winds in the stratified case and it could be interesting to test if they extend down to the surface and well into the inner layer. Last, we know that the pressure drag is controlled by the wave drag in the stable case, but we do not know if a fraction of the wave drag could and should be deposited into

the inner layer rather than being radiated away. This issue could have important consequences for the formulation of parameterizations.

The purpose of the present paper is to answer these questions in the reference case where the boundary layer is parameterized via a constant kinematic eddy viscosity ν. This case has the unique merit that, while the Couette profile with constant shear u_{0z} is an exact solution, we can handle the interactions with topography using the stratified viscous solutions derived by Hazel (1967) and Baldwin and Roberts (1970). However, a consequence of using uniform wind shear is that the "boundary layer depth" of the incident flow is infinite, it is therefore totally distinct from the "inner layer depth" over wich the waves are affected by dissipation and that scales as

$$\delta = \left(\frac{\nu L}{u_{0z}}\right)^{\frac{1}{3}}. \tag{1}$$

These simplifications of uniform viscosity and background shear were made in the literature of the late 50's by Benjamin (1959) and Smith (1973) in the context of flows over water waves and dunes respectively. Since then, we are well aware that such a "laminar" approach is an extreme idealization. A reason is that boundary layer dynamics tends to produce winds with strong shears near aloft the surface but that vary much more slowly at higher altitudes (the associated curvatures defining the "boundary layer depth" quite precisely). To defend our choice nevertheless, we can recall that in the atmosphere the low level wind shears are not only due to the boundary layer: they are also related to the large scale dynamics. This has been shown for instance in experiments done by Sheridan et al. (2007) and Doyle et al. (2011), where they observe strong shears over few kilometers above the ground. This being said, we will have to keep in mind that models with constant eddy viscosity probably overstate the significance of the low level shear stresses on the waves and pressure drag (Sykes, 1978).

The plan of the paper is as follows. In section 2 we derive the theory in the hydrostatic case. In section 3 we discuss the pressure drag and wave momentum fluxes it predicts. In section 4 we analyze the onset of downslope winds. As our theory is linear except for the lower boundary condition, our results are checked against fully nonlinear simulations in Section 5. In section 6, we discuss further the significance of works on boundary layer using constant eddy viscosity. We also discuss in this section how our results could be useful to understand the dynamics in more realistic cases. In Appendix A, we detail some aspects of the theory, and in Appendix B we provide details on the numerical implementation of the model.

2. Theory

a. Basic equations

We consider a background flow solution of the viscous equations,

$$u_0(z) = u_{0z} z;\ \rho_0(z) = \rho_r + \rho_{0z} z, \tag{2}$$

where the wind shear u_{0z} and stratification ρ_{0z} are both constant, and that is incident on a Gaussian ridge of characteristic length L and maximum height H:

$$h(x) = He^{-x^2/(2L^2)}. \tag{3}$$

Following quite conventional approaches (Beljaars et al., 1987; Belcher and Wood, 1996), we consider obstacles of small slope and use linear equations. To characterize the factors that control the dynamics we also normalize the response by introducing the "outer" scaling:

$$(x,z) = L(\overline{x},\overline{z}),\ \ (u',w') = u_{oz}L(\overline{u},\overline{w}),\ \ (p',b') = \left(\rho_r u_{0z}^2 L^2 \overline{p}, u_{0z}^2 L\overline{b}\right) \tag{4}$$

where u' and w' are the horizontal and vertical wind disturbances whereas b' is the buoyancy disturbance. With this scaling, and making the conventional "Prandtl" approximation that the vertical derivatives dominate the viscous terms, the 2D Boussinesq hydrostatic linear equations write:

$$\overline{z}\partial_{\overline{x}}\overline{u} + \overline{w} = -\partial_{\overline{x}}\overline{p} + \overline{\nu}\partial_{\overline{z}}^2\overline{u}, \tag{5a}$$

$$0 = -\partial_{\overline{z}}\overline{p} + \overline{b} \tag{5b}$$

$$\overline{z}\partial_{\overline{x}}\overline{b} + J\overline{w} = P^{-1}\overline{\nu}\partial_{\overline{z}}^2\overline{b}, \tag{5c}$$

$$\partial_{\overline{x}}\overline{u} + \partial_{\overline{z}}\overline{w} = 0. \tag{5d}$$

with no-slip boundary conditions:

$$\overline{h}(\overline{x}) + \overline{u}(\overline{x},\overline{h}) = 0,\ \overline{w}(\overline{x},\overline{h}) = 0, \text{ and } J\overline{h}(\overline{x}) + \overline{b}(\overline{x},\overline{h}) = 0 \text{ at } \overline{h} = Se^{-\overline{x}^2/2}. \tag{6}$$

In Eqs. (5)-(6),

$$J = -\frac{g\rho_{0z}}{\rho_r u_{0z}^2},\ P = \frac{\nu}{\kappa},\ S = \frac{H}{L}, \text{ and } \overline{\nu} = \frac{\nu}{u_{oz}L^2} \tag{7}$$

are a Richardson number, a Prandtl number, a slope parameter and an inverse Reynolds number respectively.

To help establish where the waves are produced and where they are dissipated we next derive from Eqs. 5 a wave-action budget. As this is not often done in mountain waves literature we recall that the interest is to define a quantity A that is quadratic (to measure the wave amplitude locally)

and conservative in the adiabatic frictionless case. For action we chose the pseudo-momentum, because its vertical flux, F^z is closely related to the mountain wave Reynolds stress[2] (see further discussions in Durran (1995) and Lott (1998)). Although the exact form of the wave action is rigorously derived when starting from Hamiltonian dynamics (Scinocca and Shepherd, 1992), we can directly use the the formula for the pseudo-momentum A derived in this paper, and derive a budget that includes dissipation by doing the formal operation:

$$\frac{\overline{b}}{J}\partial_{\overline{z}}(\text{Eq. } 5a) + \frac{\overline{u}_{\overline{z}}}{J}(\text{Eq. } 5c)\,. \tag{8}$$

After few integrations by parts one obtains,

$$\underbrace{\frac{\partial}{\partial \overline{x}}\left(\underbrace{\overline{z}\frac{\partial_{\overline{z}}\overline{u}}{J}\overline{b}}_{A} + \frac{\overline{b}^2}{2J} + \frac{\overline{u}^2}{2}\right)}_{F^x} + \frac{\partial}{\partial \overline{z}}\underbrace{\overline{u}\,\overline{w}}_{F^z} = \underbrace{\overline{v}\frac{\overline{b}}{J}\overline{\partial_{\overline{z}}^2}\partial_{\overline{z}}\overline{u} + P^{-1}\overline{v}\partial_{\overline{z}}\overline{u}\,\overline{\partial_{\overline{z}}^2}\overline{b}}_{Q}, \tag{9}$$

where F^x and F^z the horizontal and vertical components of the pseudo-momentum flux, and where Q is the production/destruction of action by dissipative processes. Note that F^x includes the horizontal advection of action by the background flow $\overline{z}A$. As we search inflow solutions that are linear, we next express them in terms of Fourier transform,

$$\overline{w}(\overline{x},\overline{z}) = \int_{-\infty}^{+\infty} \overline{\mathbf{w}}(\overline{k},\overline{z}) e^{i\overline{k}\overline{x}} d\overline{k}, \text{ where } \overline{\mathbf{w}}(\overline{k},\overline{z}) = \frac{1}{2\pi}\int_{-\infty}^{+\infty} \overline{w}(\overline{x},\overline{z}) e^{-i\overline{k}\overline{x}} d\overline{x}, \tag{10}$$

which transforms Eqs. 5 into:

$$i\overline{k}\overline{z}\,\overline{\mathbf{u}} + \overline{\mathbf{w}} = -i\overline{k}\overline{\mathbf{p}} + \overline{\nu}\partial_{\overline{z}}^2\overline{\mathbf{u}}, \tag{11a}$$

$$i\overline{k}\overline{z}\,\overline{\mathbf{b}} + J\overline{\mathbf{w}} = P^{-1}\overline{\nu}\partial_{\overline{z}}^2\overline{\mathbf{b}}, \tag{11b}$$

$$\overline{\mathbf{b}} = \partial_{\overline{z}}\overline{\mathbf{p}}\,,\;\; i\overline{k}\overline{\mathbf{u}} + \partial_{\overline{z}}\overline{\mathbf{w}} = 0. \tag{11c}$$

b. Solutions

For high Reynolds number $\overline{\nu} \ll 1$, the dynamics is inviscid at leading order. Each harmonics satisfy Eqs. 11 with $\overline{\nu} = 0$, which results in $\overline{\mathbf{w}}$ satisfying,

$$\overline{\mathbf{w}}_{\overline{z}\overline{z}} + \frac{J}{\overline{z}^2}\overline{\mathbf{w}} = 0\,. \tag{12}$$

Such equation has two solutions (Booker and Bretherton, 1967):

$$\overline{z}^{\frac{1}{2}\pm i\mu}\,, \text{ where } \mu = \sqrt{J - \frac{1}{4}}. \tag{13}$$

[2]It is actually interesting to recall that the seminal paper on wave mean flow interaction by Eliassen and Palm (1961) was about mountain waves.

When $\overline{k} > 0$ and $J > 0.25$, only the solution

$$\overline{\mathbf{w}}_I(\overline{k},\overline{z}) = \overline{z}^{1/2+i\mu}, \tag{14}$$

corresponds to a gravity wave propagating upward. The cases with $\overline{k} < 0$ are treated by complex conjugation and will not be discussed further. The cases with $J < 0.25$ are degenerated in the hydrostatic approximation because the direction of vertical propagation can not be used to distinguish between the two solutions in (13). This difficulty, which forbids to treat the weakly stratified cases (i.e., here when $J < 1/4$), will be resolved in a future non-hydrostatic treatment of the inviscid solution.

To solve the inner layer we introduce the scaling,

$$\overline{z} = \overline{\delta}\tilde{z}, (\overline{\mathbf{u}},\overline{\mathbf{w}}) = (\tilde{\mathbf{u}},\overline{\delta k}\tilde{\mathbf{w}}), (\overline{p},\overline{b}) = (\overline{\delta}\tilde{p},\tilde{b}) \text{ where } \overline{\delta} = \left(\frac{\overline{\nu}}{\overline{k}}\right)^{\frac{1}{3}}. \tag{15}$$

At leading order, it transforms the full set of non dimensional Eqs. 5 into the sixth-order set:

$$\partial_{\tilde{z}}^2\tilde{\mathbf{u}} = i\tilde{z}\tilde{\mathbf{u}} + \tilde{\mathbf{w}} + i\tilde{\mathbf{p}}, \tag{16a}$$

$$\partial_{\tilde{z}}^2\tilde{\mathbf{b}} = P\left(i\tilde{z}\tilde{\mathbf{b}} + J\tilde{\mathbf{w}}\right), \tag{16b}$$

$$\partial_{\tilde{z}}\tilde{\mathbf{w}} = -i\tilde{\mathbf{u}},\ \partial_{\tilde{z}}\tilde{\mathbf{p}} = \tilde{\mathbf{b}}. \tag{16c}$$

This set of Eqs. can be reduced to one single equation for $\tilde{\mathbf{w}}$,

$$\left(\partial_{\tilde{z}}^2 - iP\tilde{z}\right)\left(\partial_{\tilde{z}}^2 - i\tilde{z}\right)\partial_{\tilde{z}}^2\tilde{\mathbf{w}} = JP\tilde{\mathbf{w}}, \tag{17}$$

that has six independent solutions. Hazel (1967) and Baldwin and Roberts (1970) have found their asymptotic form when $\tilde{z} \to \infty$. Two grow exponentially as $\tilde{z} \to \infty$ and cannot be used (Van Duin and Kelder, 1986), the four that remain have asymptotic forms:

$$\tilde{\mathbf{w}}_1 \underset{\tilde{z}\to\infty}{\approx} \tilde{z}^{1/2-i\mu},\ \tilde{\mathbf{w}}_2 \underset{\tilde{z}\to\infty}{\approx} \tilde{z}^{1/2+i\mu},\ \tilde{\mathbf{w}}_3 \underset{\tilde{z}\to\infty}{\approx} \tilde{z}^{-5/4}e^{-\frac{2\sqrt{i}}{3}\tilde{z}^{3/2}},\ \tilde{\mathbf{w}}_4 \underset{\tilde{z}\to\infty}{\approx} \tilde{z}^{-9/4}e^{-\frac{2\sqrt{iP}}{3}\tilde{z}^{3/2}}. \tag{18}$$

In Lott (2007), these four solutions are evaluated over the entire domain $0 < \tilde{z} < \infty$, i.e. by using the asymptotic forms (18) above $\tilde{z} = 5$ and integrating down Eq. (17) from $\tilde{z} = 5$ to $\tilde{z} = 0$ with a Runge Kutta algorithm. We will essentially proceed like this here (some serious convergence issues are discussed in the appendix). We then notice that the inner function $\tilde{\mathbf{w}}_2$ matches the upward inviscid solution (14) and that $\tilde{\mathbf{w}}_3$ and $\tilde{\mathbf{w}}_4$ decay exponentially fast with altitude, which permit to tell that all the combinations of $\tilde{\mathbf{w}}_2$, $\tilde{\mathbf{w}}_3$ and $\tilde{\mathbf{w}}_4$ are uniform solutions that can match $\overline{\mathbf{w}}_I$. We therefore search a uniform approximation of the vertical velocity under the form,

$$\overline{\mathbf{w}}(\overline{k},\overline{z}) = \overline{k\delta}(k)\left[f_2(\overline{k})\tilde{\mathbf{w}}_2(\overline{z}/\overline{\delta}(\overline{k})) + f_3(\overline{k})\tilde{\mathbf{w}}_3(\overline{z}/\overline{\delta}(\overline{k})) + f_4(\overline{k})\tilde{\mathbf{w}}_4(\overline{z}/\overline{\delta}(\overline{k}))\right] \tag{19}$$

where all fields are expressed using outer variables, and with similar expression for $\overline{\mathbf{u}}$ and $\overline{\mathbf{b}}$ deduced from (11). To evaluate the unknown functions f_2, f_3 and f_4, we write the boundary conditions:

$$\overline{w}(\overline{x},\overline{h}) \approx \int_{-\infty}^{+\infty} \overline{k}\overline{\delta}(\overline{k}) \left(f_2(\overline{k})\tilde{\mathbf{w}}_2(\tilde{h}) + f_3(\overline{k})\tilde{\mathbf{w}}_3(\tilde{h}) + f_4(\overline{k})\tilde{\mathbf{w}}_4(\tilde{h}) \right) e^{i\overline{k}\overline{x}} d\overline{k} = 0, \tag{20a}$$

$$\overline{u}(\overline{x},\overline{h}) \approx \int_{-\infty}^{+\infty} \left(f_2(\overline{k})\tilde{\mathbf{u}}_2(\tilde{h}) + f_3(\overline{k})\tilde{\mathbf{u}}_3(\tilde{h}) + f_4(\overline{k})\tilde{\mathbf{u}}_4(\tilde{h}) \right) e^{i\overline{k}\overline{x}} d\overline{k} = -\overline{h}(\overline{x}), \tag{20b}$$

$$\overline{b}(\overline{x},\overline{h}) \approx \int_{-\infty}^{+\infty} \left(f_2(\overline{k})\tilde{\mathbf{b}}_2(\tilde{h}) + f_3(\overline{k})\tilde{\mathbf{b}}_3(\tilde{h}) + f_4(\overline{k})\tilde{\mathbf{b}}_4(\tilde{h}) \right) e^{i\overline{k}\overline{x}} d\overline{k} = -J\overline{h}(\overline{x}), \tag{20c}$$

where $\tilde{h}(\overline{x},\overline{k}) = \overline{h}(\overline{x})/\overline{\delta}(\overline{k})$. Once discretized in the horizontal and spectral domain, the set of equations (20) corresponds to three linear equations for $f_2(\overline{k})$, $f_3(\overline{k})$ and $f_4(\overline{k})$ that can be inverted with conventional matrix inversion routines (see appendix for more details on the numerical treatment).

3. Mountain wave fields and drags

We plot in figure 1 the flow response when the inverse Reynolds number $\overline{\nu} = 0.001$, the slope parameter $S = 0.01$, the Richardson number $J = 4$, and the Prandtl number $\mathrm{Pr} = 0.5$. This last parameter will stay unchanged in the rest of the paper: we have found moderate sensitivity of the upper wave fields to this parameter as long as its value stays around 1. In this setup, the characteristic inner layer scale is that of the dominant harmonic $\overline{k} = 1$, i.e. $\overline{\delta}(\overline{k} = 1) = \overline{\nu}^{1/3} = 0.1$, which is also the nondimensional form of the inner layer scale in (1). The inner layer scale is therefore much larger than the mountain slope.

The total wind at low level in Fig. 1a contours well the obstacle and the vertical velocity field (Fig. 1b) highlight a system of well defined upward propagating gravity waves. We notice that the stream function in Fig. 1c follows well the orography, up to at least the inner layer scale $\overline{\delta}(1) = 0.1$. For each altitudes below and around $\overline{\delta}(1)$ the streamlines are displaced vertically over distances that are near the mountain height S, and the vertical velocity when $\overline{z} \approx \overline{\delta}$ should scale as $\overline{\mathbf{w}} \approx \frac{\overline{\delta}(1)}{2} S$ to follow the streamlines. We therefore propose that the wave amplitude corresponds to the inviscid case when a uniform flow of amplitude $\overline{\delta}(1)/2$ (the average of the incident wind over the inner layer scale) is incident over a mountain of maximum height S. Far aloft and in the sheared case, the vertical velocity should therefore scale as $\overline{\mathbf{w}} = 0 \left(\frac{\sqrt{\overline{z}\overline{\delta}(1)}}{2} S \right)$, where the square root corresponds to the $\frac{1}{2}$ factor in the exponent of the inviscid solution (14). This qualitative argument tells that the amplitude of $\overline{\mathbf{w}}$ should be around $S\overline{\delta}(1)/2 = 5.10^{-4}$ at $\overline{z} = 1$, which is in qualitative agreement with what is found in Fig. 1b.

We follow this line of qualitative reasoning and propose as predictor of the wave momentum flux and mountain pressure drag,

$$\overline{\overline{u}\,\overline{w}}(\overline{z}) = \int_{-\infty}^{+\infty} \overline{u}(\overline{x},\overline{z})\overline{w}(\overline{x},\overline{z})d\overline{x},\ Dr = -\int_{-\infty}^{+\infty} \overline{p}(\overline{x},\overline{h})\frac{\partial \overline{h}}{\partial \overline{x}}d\overline{x}, \tag{21}$$

the inviscid linear hydrostatic pressure drag produced by a uniform wind of intensity $\overline{\delta}(1)/2$ incident on the orography given by $\overline{h}(\overline{x})$ in (6), and which exact value is

$$-\frac{\overline{\delta}(1)}{2}\sqrt{J}S^2 = -Dr_{GWP}. \tag{22}$$

Henceforth, we will refer to Dr_{GWP} as the gravity wave drag amplitude predictor. Figure 2 shows that this predictor is a good estimate for the drag given by the theoretical model for a very large range of J and slope S. We conclude that the pressure drag is well controlled by the inviscid GW dynamics outside of the inner layer, the GWs being forced by the ondulations of the inner layer produced by the mountain. This picture where the inner layer forces the (inviscid) dynamics aloft, and that the pressure drag is ultimately controlled by this inviscid dynamics follows the general principle of boundary layer theories that pressure is approximately constant across the inner layer.

This predictor of the surface pressure drag is nevertheless misleading if we take it as a measure of the effect of the mountain on the large-scale flow, as is generally done in mountain meteorology. The reason is that, in a steady state, our waves are forced indirectly by the distortion of the inner layer produced by the mountain rather than directly by the mountain as in the inviscid case. To establish this, we return to Fig. 1d where we plotted the waves pseudomomentum flux vector. Aloft the inner layer this flux clearly points down, as expected for mountain GWs propagating upward (Durran, 1995; Lott, 1998), but within the inner layer, it points very strongly from the upstream sector toward the downstream sector. This is to be contrasted with the inviscid case where this flux goes through the surface and produces an exchange of momentum between the fluid and the solid ground.

This result suggests that the acceleration that balances the gravity wave drag is not communicated to the earth surface but rather to the inner layer. This last statement is confirmed in Fig. 3a where we plot the wave stress as a function of altitude. The wave stress is null at the surface, increases with altitude before reaching a constant value at altitudes above $\overline{z} > 5\overline{\delta}(1)$ typically. As is often the case for viscous boundary layers, the depth over which dissipation is significant seems to be around 5 times the inner layer scale $\overline{\delta}(1)$, so we will systematically make the distinction between the inner layer scale ($\overline{\delta}(1)$) and the inner layer depth (around $5\overline{\delta}(1)$). The flux emitted at the top of the inner layer (above $5\overline{\delta}(1)$) is around half the pressure drag, at least when when $J \approx 1$. Such value stays comparable to the theoretical drag but suggests that substantial wave dissipation occurs when the wave travels vertically through the inner layer (in our scenario where the waves

are forced around $\overline{\delta}(1)$). This erosion of the pressure drag toward the gravity wave stress is even more significant when J increases. This is again consistent with a qualitative argument: for large values of J, the waves oscillate more rapidly in the vertical according to Eq. (14) and are more affected by viscous dissipation. This difficulty in converting the pressure drag into a momentum flux as stability increases makes that for $J > 4$ typically, there is a minimum in $\overline{\overline{u}\,\overline{w}}$ in the middle of the inner layer (between $2\overline{\delta}(1)$ and $5\overline{\delta}(1)$): part of the momentum given to the inner layer near the surface is restored back around the top of the inner layer.

To understand what can replace the Reynolds stress to balance the pressure drag, it is important to return to the initial Eliassen and Palm (1961)'s paper where it is shown that the momentum flux is related to the pressure force exerted in the horizontal direction on an undulating surface. In the linear stationary case, this relation is obtained by multiplying a momentum equation (Eq. 5a in our case) by the vertical displacement of streamlines $\overline{\eta}$ and after integration by part over $\overline{x}$ we get

$$\overline{\overline{u}\,\overline{w}} = -\overline{\overline{p}\partial_{\overline{x}}\overline{\eta}} - \overline{\nu}\,\overline{\left(\overline{\eta}\,\partial^2_{\overline{z}}\overline{u}\right)}\,, \text{ where } \overline{z}\partial_{\overline{x}}\overline{\eta} = \overline{w}. \tag{23}$$

In the inviscid case the pressure stress equals the Reynolds stress, but this is no longer true in the viscous scenario where dissipation plays a non negligible role. To illustrate how dissipation becomes significant for small slopes, we plot the two terms on the right hand side and their sum for three values of J in Fig. 3b. After verification that the sum in Fig. 3b exactly equals the Reynolds stresses in Fig. 3a, we see that Reynolds stress and the pressure drag only coincide well above the boundary layer. Near the surface and in the lower part of the inner layer, the pressure drag is almost entirely balanced by the viscous drag.

This erosion of the pressure drag toward the wave Reynolds stress is summarized in Fig. 4a where we plot the Reynolds stress emitted in $\overline{z} \to \infty$ normalized by the predictor Dr_{GWP}. As already discussed, the emitted flux is half the predicted drag, but this result becomes sensitive to the stability J: when J is large, the emitted flux almost vanishes. This erosion of the pressure drag toward the Reynolds stress for large J is less pronounced if we consider the minimum values in Fig. 4b. These minima are in general located in the middle of the inner layer (i.e. above $\overline{z} = \overline{\delta}(1)$ and below $5\overline{\delta}(1)$, (see Fig. 3a) such that for large J some GW deceleration should be applied directly around the top of the boundary layer (which we locate at $5\overline{\delta}(1)$).

4. Non-separated blocking and downslope winds

To analyze what occurs in nonlinear situations we next consider cases where the slope S becomes comparable to the boundary layer scale $\overline{\delta}(1)$. As a first example, the simulation in Fig. 5 corresponds to that in Fig. 1 but with $S = 0.15$ instead of $S = 0.01$. We readily notice that the total wind (Fig. 5a) presents an downslope/upslope asymmetry that is almost absent in Fig. 1a.

The vertical velocity is around 30 times larger than in the small slope case, i.e. 3 times larger than what should have been obtained if we applied a linear ratio of the slopes (Figs. 5b and 1b). The asymmetry in the winds is also visible in the stream function in Fig. 5c, with a pronounced descent on the lee side. Finally, the largest differences are maybe in the pseudo-momentum flux vector in Fig. 5d. Now that the obstacle penetrates well into the boundary layer, there is a substantial pseudo-momentum flux across the surface. In opposition to the inviscid case (Lott, 1998) we did not identify clear relations between this flux and the mountain drag, except that the total flux across the surface is of the same order of magnitude as the mountain drag when the slope approaches the inner layer scale.

To appreciate more systematically the changes occuring when the slope parameter increases as a function of stability, we plot in Fig. 6 the vertical velocity fields for different valuse of S and J. The panels in the top row are for a slope that is small compared to the inner layer scale ($S = 0.02 < \overline{\delta}(1)$) and those in the bottom row for a slope that compares to it ($S = 0.15 \approx \overline{\delta}(1)$). The contour interval stays the same between all panels with given slope, consistent with the fact that the kinematic boundary conditions are independent of J (see Eq. 6). Between the upper and lower row where the slope changes, the contour interval changes with a factor proportional to the slope ratio, i.e. following a linear relation. For the small slope cases when J increases (Figs. 6a, 6b, and 6c), one sees that the wave amplitude in the far field decreases with J. If we recall that the vertical scale of variations of our solutions is inversely proportional to J, larger values of J correspond to cases where the solutions oscillate more in the vertical direction, these plots are therefore consistent with the interpretation that with large J the waves are more dissipated when they travel through the inner layer. When the slope increases, a second interesting behavior is worth noticing. When $J = 1$ there are little differences between the patterns in Figs. 6a and 6d, which means that amplitudes varies linearly with S (remember that the contour interval varies linearly with S between the upper and lower row). Again, we know since Lott (2016) and Damiens et al. (2018) that this is also related to the vertical scale of the waves: strong nonlinear effects enter the dynamics via the surface boundary condition and when the vertical wavelength at the top of the obstacle compares to the vertical wavenumber, a criteria that corresponds to $J > 1$. As we see in the following panels in Figs. 6e and 6f these nonlinear effects become substantial: for a given slope the wave amplitude now increases when J increases. In addition to the enhaced emission due to nonlinearities, it is also plausible that the wave dissipation through the inner layer is less intense because the level of emission is located at a higher altitude than for smaller slopes. If we return to the emitted momentum fluxes in Fig. 4, a consequence of these enhanced emission and reduced dissipation when the slope increase and for large J is that the inviscid predictor of the momentum flux Dr_{GWP} becomes more and more accurate (see the grey dotted line in Figs. 4a and 4b).

If we now return to the total winds in Fig. 7 we also see that for large slope and large J, the winds along the upslope flank of the mountain become small compared to the downslope winds, an asymmetry that increases with both S and J. More specifically, when $J = 1$ (Fig. 7a) the flow contours the obstacle: the flow is upward on the upwind side and downward on the downwind side with little asymmetry in amplitudes, a behavior that is little affected by the increase in the slope in Fig. 7d. When J increase and still for small slope in Figs. 7b and 7c some upwind/downwind asymmetry starts to occur but stays limited: there is still substantial ascent on the upstream side of the obstacle. This ascent is actually not confined to the lower layers but extends up to at least twice the mountain slope. When the slope is larger (Figs. 7e and 7f), the upwind ascent is much smaller than the downwind descent. The downwind descent extends well along the downwind slope whereas along the upwind slope the total wind is very small. We call this situation a "non-separated" blocking because it is produced by linear inflow dynamics.

To quantify the dependence on S and J more systematically in terms of upstream blocking and downslope winds, we plot in Fig. 8 the ratio between the wind amplitude along the downwind slope and the upwind slope of the ridge defined as

$$\underbrace{\mathrm{Max}}_{\overline{z}<\frac{2\overline{h}}{3},0<\overline{x}<2} \sqrt{(\overline{z}+\overline{u})^2+\overline{w}^2} \Bigg/ \underbrace{\mathrm{Max}}_{\overline{z}<\frac{2\overline{h}}{3},-2<\overline{x}<0} \sqrt{(\overline{z}+\overline{u})^2+\overline{w}^2}\ . \tag{24}$$

This ratio emphasizes more the downslope-upslope asymmetry than the criteria used in Lott (2016) where only the downslope wind amplitude was measured in relation with the wind at the top of the hill. The reason is that here the wind at the top of the hill is null so this measure makes little sense. Here the ratio measures the upstream flow blocking as much as the downslope wind intensification and we see that it can easily reach values around 4 or 5 for slopes near the boundary layer depth $\delta(1) = 0.1$ and when J is sufficiently large. It always stays near 1 for small slopes and essentially increases with J and S as expected.

5. Validation with a fully nonlinear model

To validate our results we now use the ocean general circulation model developed at MIT (MITgcm) (Marshall et al., 1997) and which solves the fully nonlinear Boussinesq hydrostatic equations on a cartesian mesh with a staggered Arakawa C-grid. We set the shape of the topography to a Gaussian (Eq. 3) and take $L = 1$ km and $H = 150$ m which yield $S = 0.15$. Cells near the bottom are cut with the partial cells strategy (Adcroft et al., 1997) with $hFacmin = 0.1$ (if a fraction of the cell is less than $hFacMin$ then it is rounded to the nearer of 0 or $hFacMin$). The total domain horizontal size is 60 km with a stretched grid near the topography: the minimum and maximum grid size are 60 m and 600 m respectively. We use a sponge layer at the lateral boundaries to relax

the dynamic variables (momentum and temperature) to the prescribed upstream profiles (2). The relaxation time scale is 100 s in the innermost point of the sponge layer and 10 s in the outermost point of the sponge layer. We also use a stretched grid in the vertical with maximum resolution of 5.6 m at the topography and 415 m at the top of the domain. The total height of the domain is 50 km, and we use a sponge layer above 10 km with a relaxation time scale that varies quadratically with a minimum time scale of 10 s at the uppermost grid point (and infinite relaxation time scale at 10 km). We use a constant wind shear ($u_{0_z} = 10^{-3}$ s^{-1}) and constant vertical temperature gradient. The temperature is related to the density via a linear equation of state and we adjust the vertical stratification N^2 to match the non dimensional values of J: from $N^2 = 5 \times 10^{-7}$ s^{-2} ($J = 0.5$) to $N^2 = 1.6 \times 10^{-5}$ s^{-2} ($J = 16$). We use no-slip boundary conditions for momentum at the topography and we set the bottom temperature to $T = 0^o$ C (we modified the code to get a temperature flux at the boundary to ensure that the temperature at the topography is constant). The horizontal and vertical viscosities for momentum are set to 1 m^2 s^{-1}. The vertical and horizontal coefficients of diffusivity for temperature are set to 2 m^2 s^{-1}. We also added a horizontal bi-harmonic damping with a coefficient of 2×10^3 m^4 s^{-1} for both the temperature and momentum in order to damp grid scale noise generated at the topography. The time step is 0.5 *s*. The model is integrated forward in time until we reach a steady state (usually less than one day).

The results for the vertical velocity field in Figs. 9a, 9b, and 9c, reproduce reasonably well the corresponding predictions from the theory in Figs. 6d, Figs. 6e, and 6f respectively. The horizontal scale and vertical variations are well reproduced, the amplitudes in the MITgcm are about 10% smaller near $\overline{z} = 1$ than in the theory, a difference we attribute to numerical dissipation that are not easy to control. The results for the winds at low level in Figs. 9d, 9e, and 9f are also consistent with those from the theory in Figs. 7d, Figs. 7e, and 7f respectively. The flow in the MITgcm presents the upstream/downstream symmetry predicted by theory when $J = 1$ Fig. 9a, and stronger downslope than upslope winds when $J = 9$ and $J = 16$. We conclude that there is a good agreement between the global indexes defined in the theoretical model and the fully non-linear model (see for instance the comparison of the emitted wave fluxes in Figs. 3a and 3b, or of the downslope windstorm index in Fig. 8). The only noticeable difference is on the pressure drag in Fig. 2, the MITgcm predicts a larger drag than in the theory. We have tried to understand the causes of the differences, but find it difficult to correct the error. A reason is that the major differences between the theory and the MITgcm are essentially located near the surface (not shown), i.e. at places where viscous stress equals the Reynolds stress and where the stepwise treatment of the lower boundary can produce grid-scale irregularities on these fields. As such irregularities are likely to be damped out by dissipation as we move away from the surface, we can speculate that these

low level differences on the velocity shears and pressure are not significant in the context of the interactions between the waves and the large scale flow at upper levels.

6. Conclusion

In dynamical meteorology and oceanography, solutions with constant viscosity have always been a starting points to understand phenomena that involve the interaction between the surface and the boundary layer. Examples are numerous, from the Ekman et al. (1905) solutions systematically given in textbook, the Prandtl (1952) model for katabatic winds, the inclusion of a boundary layer in the Miles theory for the generation of oceanic waves (Benjamin, 1959), or in theories of sand ripples and dunes formation (Engelund, 1970) (see also Fowler (2001)). In waves and dune theories, the fact that the near surface wind profiles play a crucial role in the dynamics was early recognized (Miles, 1957; Benjamin, 1959) , and a first difficulty consisted in solving the fourth order Orr-Sommerfield equation and to introduce a corrugated bottom at the surface (Fowler, 2001). A difficulty arises if one wishes to introduce stratification: the equation to solve becomes of the sixth order (see Eq. 17). This difficulty plus the facts that a constant eddy viscosity is a crude approximations of the turbulence in actual boundary layers, are two reasons why the viscous problem is not often treated in the stratified case. When it is, the techniques used are extremely involved (see for instance the introduction of "triple decks" in Sykes (1978)), and does not permit to derive uniform approximations of the solutions over the entire domain. As this last remark also holds for more sophisticated eddy viscosity closure, it is fair to say that theories failed so far in predicting the vertical profiles of the waves Reynolds stress, a quantity that is central in mountain meteorology. For these reasons but also because more and more papers in mountain meteorology call for a better understanding of the interaction between boundary layers and mountain waves, we found useful to solve the viscous mountain wave problem theoretically, and verify the theory with a fully nonlinear model (here the MITgcm). Note that in the context of stratified oceanic boundary layers over corrugate and tilted slopes, a recent paper by Passaggia et al. (2014) shares the same concern.

Once given this context, what are the messages that could be useful in a more realistic context? The first is probably that pressure drag and wave Reynolds stress are well predicted by inviscid theory and if we take for the incident flow, its value averaged over the inner layer depth. This depth has a definition that can be generalized, at least conceptually. For instance, if the boundary layer scheme uses first order closure with vertical diffusion coefficients, the coefficients and tendencies can be linearized around the large-scale resolved state. If we consider a small perturbation of given horizontal scale, the inner layer depth of interest is that where advection by the resolved wind equals the disturbance in boundary layer tendency. These predictions of the drag and waves

Reynolds stress remain valid until the mountain height equals the inner layer scale. Our theory does not go beyond that height. For higher mountains we should probably average the incident flow over the mountain height to obtain realistic predictions. Actually, this is what we find with our model when imposing free slip boundary condition in $\overline{z} = \overline{h}$, i.e. in an inviscid approximation where the boundary layer depth is drastically reduced (not shown).

For large values of the stratification, we also find that a good fraction of the stress is dissipated near the top of the inner layer, simply because the waves have shorter vertical wavelength and are more dissipated there. This effect is mitigated when the top of the hill is near the top of the inner layer scale again, but suggests that a good fraction of the mountain wave drag should be given back to the flow near the top of the inner layer. Another interesting result concerns the source of the mountain wave stress. When the mountain is well inside the inner layer, the wave stress is in good part extracted from the inner layer itself rather than from the solid earth as in the inviscid case. When the mountain slope approaches the inner layer depth this result is less applicable and a good part of the pseudo momentum flux is directed toward the surface as in the inviscid case (Durran, 1995; Lott, 1998).

Our results could also be used to provide alternative views concerning the dynamics of upstream blocking and downslope winds. They occur through a near surface critical level dynamics and without upper level wave breaking (remember that our theory is linear inside the flow) providing that the flow is stable $J > 1$, and that the mountain slope is near the inner layer scale. This confirms the results in Lott (2016) and Damiens et al. (2018) who predicted these behaviors using simpler theories and using simulations with WRF including more sophisticated boundary layers. Another important result concern the structure of the inner layer itself: the downslope winds penetrate well into the inner it, as shows for instance Fig. 7 when $J = 9$ or $J = 16$.

Last, for all the results presented here, we have neglected that the mountain gravity waves necessarily return to the surface in the constant shear case: they are all trapped, and this effect should be taken into account to give a more realistic treatment of the constant shear case. To take this into account within our theoretical framework we need to reject the hydrostatic approximation and we have to treat the inviscid solution in terms of Hankel functions (Keller, 1994), a solution we will describe in a future paper. Note that such subsequent development will also allow us to treat the non-stratified situation and describe the transition from the neutral to the stratified case. Here we wanted to treat the hydrostatic case first because an extremely rich dynamics already occur at low level and we do not need to attribute this dynamics to the fact that all the harmonics are trapped.

In this paper also, the background shear flow is constant, which corresponds to a boundary layer flow of infinite depth. Hence, even though we insist on using the terminology that the dynamics introduces an ”inner” layer scale, it has to be clearly distinguished from the plausible presence

of a "boundary layer", where the incident wind present large curvature. Again, we can treat such problem with our formalism by imposing background flow with non-zero curvature, a situation that can introduced trapped lee waves in the non-hyrostatic case (Soufflet et al., 2019).

APPENDIX

A1. Pre-conditioning of the viscous solution

To evaluate $\tilde{\mathbf{w}}_2$, $\tilde{\mathbf{w}}_3$, and $\tilde{\mathbf{w}}_4$ we proceed as in Lott (2007), take the asymptotic forms in (18) when $\tilde{z} > 5$ and integrate down to $\tilde{z} = 0$ with a Runge-Kutta algorithm. Nevertheless these solutions are ill-conditioned when it comes to the inversion of the boundary condition, essentially because $\tilde{\mathbf{w}}_3$ and $\tilde{\mathbf{w}}_4$ vary exponentially with altitude (see (18)). To circumvent this difficulty, rather than $\tilde{\mathbf{w}}_2$, $\tilde{\mathbf{w}}_3$, and $\tilde{\mathbf{w}}_4$ we have used 3 solutions $\tilde{\mathbf{w}}_a$, $\tilde{\mathbf{w}}_b$, and $\tilde{\mathbf{w}}_c$ which asymptotic behavior for $\tilde{z} \to \infty$ all match the inviscid solution $\overline{\mathbf{w}}_I$ when $\overline{z} \to 0$, but which do not grow exponentially fast when $\tilde{z} \to 0$:

$$\tilde{\mathbf{w}}_a(\tilde{z}) = \tilde{\mathbf{w}}_2(\tilde{z}) + \tilde{a}_3\tilde{\mathbf{w}}_3(\tilde{z}) + \tilde{a}_4\tilde{\mathbf{w}}_4(\tilde{z}) \tag{A1a}$$

$$\tilde{\mathbf{w}}_b(\tilde{z}) = \tilde{\mathbf{w}}_2(\tilde{z}) + \tilde{b}_3\tilde{\mathbf{w}}_3(\tilde{z}) + \tilde{b}_4\tilde{\mathbf{w}}_4(\tilde{z}) \tag{A1b}$$

$$\tilde{\mathbf{w}}_c(\tilde{z}) = \tilde{\mathbf{w}}_2(\tilde{z}) + \tilde{c}_3(\overline{k})(\tilde{z}) + \tilde{c}_4\tilde{\mathbf{w}}_4(\tilde{z}). \tag{A1c}$$

The three pairs $(\tilde{a}_3, \tilde{a}_4)$, $(\tilde{b}_3, \tilde{b}_4)$, $(\tilde{c}_3, \tilde{c}_4)$ are then chosen so that $(\partial_{\tilde{z}}\tilde{\mathbf{u}}_a(0), \partial_{\tilde{z}}\tilde{\mathbf{b}}_a(0)) = (0,0)$, $(\partial_{\tilde{z}}\tilde{\mathbf{u}}_b(0), \tilde{\mathbf{p}}_b(0)) = (0,0)$, and $(\partial_{\tilde{z}}\tilde{\mathbf{b}}_c(0), \tilde{\mathbf{p}}_c(0)) = (0,0)$ respectively. These three solutions are shown in Fig. 10 for $J = 1$ and $Pr = 0.5$, they show moderate variations with inner altitude $\tilde{z}$, the exponential behavior of $\tilde{\mathbf{w}}_3$ and $\tilde{\mathbf{w}}_4$ has clearly been mitigated by adopting finite amplitudes values for the variables and their derivatives at the surface. The boundary condition is then satisfied by writing,

$$\overline{w}(\overline{x},\overline{h}) \approx \int_{-\infty}^{+\infty} \overline{k}\overline{\delta}(\overline{k}) \left(f_a(\overline{k})\tilde{\mathbf{w}}_a(\tilde{h}) + f_b(\overline{k})\tilde{\mathbf{w}}_b(\tilde{h}) + f_c(\overline{k})\tilde{\mathbf{w}}_c(\tilde{h}) \right) e^{i\overline{k}\overline{x}} d\overline{k} = 0, \tag{A2a}$$

$$\overline{u}(\overline{x},\overline{h}) \approx \int_{-\infty}^{+\infty} \left(f_a(\overline{k})\tilde{\mathbf{u}}_a(\tilde{h}) + f_b(\overline{k})\tilde{\mathbf{u}}_b(\tilde{h}) + f_c(\overline{k})\tilde{\mathbf{u}}_c(\tilde{h}) \right) e^{i\overline{k}\overline{x}} d\overline{k} = -\overline{h}(\overline{x}), \tag{A2b}$$

$$\overline{b}(\overline{x},\overline{h}) \approx \int_{-\infty}^{+\infty} \left(f_a(\overline{k})\tilde{\mathbf{b}}_a(\tilde{h}) + f_b(\overline{k})\tilde{\mathbf{b}}_b(\tilde{h}) + f_c(\overline{k})\tilde{\mathbf{b}}_c(\tilde{h}) \right) e^{i\overline{k}\overline{x}} d\overline{k} = -J\overline{h}(\overline{x}), \tag{A2c}$$

where $\tilde{h}(\overline{x},\overline{k}) = \overline{h}(\overline{x}/)\overline{\delta}(\overline{k})$. Once discretized in the horizontal and spectral domain, the set of equations (20) corresponds to three linear equations involving nine matrices (for instance one of the matrix has for components $\overline{k}_j\overline{\delta}(\overline{k}_j)\tilde{\mathbf{w}}_a(\tilde{h}_{ij})e^{i\overline{k}_j\overline{x}_i}d\overline{k}$) and three unknown vectors (with components $f_a(\overline{k}_j)$, $f_b(\overline{k}_j)$, and $f_c(\overline{k}_j)$) that can be inverted with conventional matrix inversion routines.

Still in this formalism, the uniform approximation of $\overline{\mathbf{w}}$ in (19) writes,

$$\overline{\mathbf{w}}(\overline{k},\overline{z}) = \overline{k\delta}(k)\left[f_a(\overline{k})\tilde{\mathbf{w}}_a(\overline{k},\overline{z}/\overline{\delta}(\overline{k})) + f_b(\overline{k})\tilde{\mathbf{w}}_b(\overline{k},\overline{z}/\overline{\delta}(\overline{k})) + f_c(\overline{k})\tilde{\mathbf{w}}_c(\overline{k},\overline{z}/\overline{\delta}(\overline{k}))\right] \tag{A3}$$

again with similar expression for $\overline{\mathbf{u}}$ and $\overline{\mathbf{b}}$.

A2. Numerical resolution

To solve numerically our problem we always take a domain of length $\overline{X} = 100$ spanned by $N = 1024$ points, which corresponds to a spectral resolution around $d\overline{k} \approx 0.01$ and a spatial resolution around $d\overline{x} \approx 0.1$. In the vertical we take grids of maximum depth $\overline{Z} = 3$ and smoothly varying vertical resolution. The variable resolution is such that for $\overline{z} > 10S$ the grid spacing $dz \approx 0.03$ whereas near around and below the mountain top $dz \approx S/10$. We will then systematically vary the other two non dimensional parameters of the problem S, and J.

Concerning the variations in slope S, we have to assume that the mountain is well in the boundary layer, a condition that needs to be satisfied for each harmonics. Although this pauses a theoretical problem since in the infinite Fourier integrals $\overline{k}$ can become extremely large (and $\overline{\delta}(\overline{k})$ very small) it can be handled numerically once fixed the horizontal scale of the domain over which Fourier series approximate Fourier transform and once fixed the number of horizontal grid points. More specifically, if $\overline{k}_{max} = N\pi/X$, the condition that the associated boundary layer depth is larger than the mountain top is $\frac{S}{\overline{\delta}(\overline{k}_{max})} \approx 1$ or less. Nevertheless, and for moderately large domain length $\overline{X}$ it happens that it is sufficient to satisfy this condition for the dominant wavenumbers, i.e. to satisfy $\frac{S}{\overline{\delta}(1)} \not> 1$. This guaranties that the dominant harmonics forced by the obstacle are still well viscous near the mountain top. In this case, numerical convergence was found up to around $S \approx 0.15$.

Acknowledgement

This work was supported by the Laboratoire de Recherche Conventionn Yves Rocard, a collaborative unit between CEA and Ecole Normale Supérieure.

References

Adcroft, A., C. Hill, and J. Marshall, 1997: Representation of topography by shaved cells in a height coordinate ocean model. *Mon. Wea. Rev.*, **125**, 2293–2315, doi:10.1175/1520-0493(1997)125⟨2293:ROTBSC⟩2.0.CO;2.

Ayotte, K., 2008: Computational modelling for wind energy assessment. *Journal of Wind Engineering and Industrial Aerodynamics*, 1571–1590, doi:10.1016/j.jweia.2008.02.002.

Baldwin, P., and P. H. Roberts, 1970: The critical layer in stratified shear flow. *Mathematika*, **17**, 102–119.

Belcher, S. E., and N. Wood, 1996: Form and wave drag due to stably stratified turbulent flow over low ridges. *Quart. J. Roy. Meteor. Soc.*, **122**, 863–902.

Beljaars, A., J. Walmsley, and P. Taylor, 1987: A mixed spectral finite-difference model for neutrally stratified boundary-layer flow over roughness changes and topography. *Boundary-Layer Meteorology*, **38 (3)**, 273–303.

Beljaars, A. C. M., A. R. Brown, and N. Wood, 2004: A new parametrization of turbulent orographic form drag. *Quarterly Journal of the Royal Meteorological Society*, **130 (599)**, 1327–1347.

Benjamin, T. B., 1959: Shearing flow over a wavy boundary. *Journal of Fluid Mechanics*, **6 (2)**, 161–205.

Booker, J. R., and F. P. Bretherton, 1967: The critical layer for internal gravity waves in a shear flow. *J. Fluid Mech.*, **27**, 102–109, doi:http://dx.doi.org/10.1017/S0022112067000515.

Charru, F., B. Andreotti, and P. Claudin, 2012: Sand ripples and dunes. *Annu. Rev. Fluid Mech.*, **45**, 469–493, doi:10.1146/annurev-fluid-011212-140806.

Damiens, F., F. Lott, C. Millet, and R. Plougonven, 2018: An adiabatic foehn effect. *Quart. J. Roy. Meteor. Soc.*, **144**, 1369–1381, doi:10.1002/qj.3272.

Doyle, J. D., and Coauthors, 2011: An intercomparison of t-rex mountain-wave simulations and implications for mesoscale predictability. *Monthly weather review*, **139 (9)**, 2811–2831.

Durran, D. R., 1990: Mountain waves and downslope winds. *AMS Meteorological Monographs*, **23**, 59–83.

Durran, D. R., 1995: Pseudomomentum diagnostics for two-dimensional stratified compressible flow. *Journal of the atmospheric sciences*, **52 (22)**, 3997–4009.

Ekman, V. W., and Coauthors, 1905: On the influence of the earth's rotation on ocean-currents. *Almqvist & Wiksells boktryckeri, A.-B.,*.

Eliassen, A., and E. Palm, 1961: On the transfer of energy in stationary mountain waves. *Geofys. Publ.*, **22**, 1–23.

Engelund, F., 1970: Instability of erodible beds. *Journal of Fluid Mechanics*, **42 (2)**, 225–244.

Fowler, A., 2001: Dunes and drumlins. *Geomorphological fluid mechanics*, Springer, 430–454.

Hazel, P., 1967: The effect of viscosity and heat conduction on internal gravity waves at a critical level. *Journal of Fluid Mechanics*, **30 (4)**, 775–783.

Hunt, J. C. R., S. Leibovich, and K. J. Richards, 1988: Turbulent shear flows over low hills. *Quart. J. Roy. Meteor. Soc.*, **114**, 1435–1470.

Jackson, P. S., and J. C. R. Hunt, 1975: Turbulent wind flow over low hill. *Quart. J. Roy. Meteor. Soc.*, **101**, 929–955.

Jiang, Q., J. D. Doyle, and R. B. Smith, 2006: Interaction between trapped waves and boundary layers. *J. Atmos. Sci.*, **63**, 617–633, doi:http://dx.doi.org/10.1175/JAS3640.1.

Keller, T. L., 1994: Implications of the hydrostatic assumption on atmospheric gravity waves. *Journal of the atmospheric sciences*, **51 (13)**, 1915–1929.

Lott, F., 1998: Linear mountain drag and averaged pseudo-momentum flux profiles in the presence of trapped lee waves. *Tellus A: Dynamic Meteorology and Oceanography*, **50 (1)**, 12–25.

Lott, F., 2007: The reflection of a stationary gravity wave by a viscous boundary layer. *J. Atmos. Sci.*, **139**, 3363–3371, doi:http://dx.doi.org/10.1175/JAS4020.1.

Lott, F., 2016: A new theory for downslope windstorms and trapped lee waves. *J. Atmos. Sci.*, **73**, 3585–3597, doi:doi:10.1175/JAS-D-15-0342.1.

Lott, F., and M. Miller, 1997: A new subgrid scale orographic drag parameterization; its testing in the ecmwf model. *Quart. J. Roy. Meteor. Soc.*, **123**, 101–127.

Marshall, J., A. Adcroft, C. Hill, L. Perelman, and C. Heisey, 1997: A finite-volume, incompressible Navier Stokes model for studies of the ocean on parallel computers. *J. Geophys. Res.*, **102**, 5753–5766, doi:10.1029/96JC02775.

Miles, J. W., 1957: On the generation of surface waves by shear flows. *Journal of Fluid Mechanics*, **3 (2)**, 185–204.

Olafsson, H., and P. Bougeault, 1997: The effect of rotation and surface friction on orographic drag. *J. Atmos. Sci.*, **54**, 193–210.

Passaggia, P.-Y., P. Meunier, and S. Le Dizes, 2014: Response of a stratified boundary layer on a tilted wall to surface undulations. *Journal of Fluid Mechanics*, **751**, 663684, doi:10.1017/jfm.2014.296.

Pithan, F., T. G. Shepherd, G. Zappa, and I. Sandu, 2016: Missing orographic drag leads to climate model biases in jet streams, blocking and storm tracks. *Geophysical Research Letters*, **43**, 7231–7240.

Prandtl, L., 1952: Essentials of fluid dynamics blackie. *London-Glasgow, 452p*.

559 Richard, E., P. Mascart, and E. C. Nickerson, 1989: The role of surface friction in downslope
560 windstorms. *J. Appl. Meteor.*, **28**, 241–251.

561 Sandu, I., P. Bechtold, A. Beljaars, A. Bozzo, F. Pithan, T. Shepherd, and A. Zadra, 2015: Im-
562 pacts of parameterized orographic drag on the northern hemisphere winter circulation, jour-
563 nal of advances in modeling earth systems. *J. Adv. Model. Earth Syst.*, **8**, 196–211, doi:
564 DOI:10.1002/2015MS000564.

565 Scinocca, J., and T. Shepherd, 1992: Nonlinear wave-activity conservation laws and hamilto-
566 nian structure for the two-dimensional anelastic equations. *Journal of the atmospheric sciences*,
567 **49 (1)**, 5–28.

568 Sheridan, P., S. Vosper, and P. Brown, 2017: Mountain waves in high resolution forecast models:
569 Automated diagnostics of wave severity and impact on surface winds. *Atmosphere*, **8 (1)**, 24.

570 Sheridan, P. F., V. Horlacherxi, G. G. Rooney, P. Hignett, S. D. Mobbs, and S. Vosper, 2007:
571 Influence of lee waves on the near surface flow downwind of the pennines. *Quart. J. Roy. Meteor.*
572 *Soc.*, **133**, 1353–1369, doi:10.100a/2qj.110.

573 Smith, F., 1973: Laminar flow over a small hump on a flat plate. *Journal of Fluid Mechanics*,
574 **57 (4)**, 803–824.

575 Smith, R. B., Q. Jiang, and J. D. Doyle, 2006: A theory of gravity wave absorption by a boundary
576 layer. *J. Atmos. Sci.*, **63**, 774–781, doi:http://dx.doi.org/10.1175/JAS3631.1.

577 Smith, R. B., S. Skubis, J. D. Doyle, A. S. Broad, C. Kiemle, and H. Volkert, 2002: Mountain
578 waves over the mont blanc: Influence of a stagnant boundary layer. *J. Atmos. Sci.*, **59**, 2073–
579 2092.

580 Soufflet, C., F. Lott, and F. Damiens, 2019: Trapped mountain waves with critical level just below
581 the surface. *Quart. J. Roy. Meteor. Soc.*, **Submitted**.

582 Sykes, R., 1978: Stratification effects in boundary layer flow over hills. *Proceedings of the Royal*
583 *Society of London. A. Mathematical and Physical Sciences*, **361 (1705)**, 225–243.

584 Van Duin, C. A., and H. Kelder, 1986: Internal gravity waves in shear flows at large reynolds
585 number. *Journal of Fluid Mechanics*, **169**, 293–306.

586 Wood, N., A. Brown, and F. Hewer, 2001: Parameterizing the effects of orography on the boundary
587 layer: an alternative to effective roughness lengths. *Quart. J. Roy. Meteor. Soc.*, **127**, 759–777.

588 Wood, N., and P. Mason, 1993: The pressure force induced by neutral, turbulent flow over hills.
589 *Quart. J. Roy. Meteor. Soc.*, **119**, 1233–1267.

LIST OF FIGURES

Fig. 1. Physical fields predicted by the theory in the hydrostatic case and when $J = 4$, $S = 0.01$, $\overline{\delta} = 0.1$. a) Total wind vector $(\overline{z}+\overline{u},\overline{w})$, b) vertical wind $\overline{w}$; c) total stream function $\overline{\psi}$ defined by: $\partial_{\overline{z}}\overline{\psi} = \overline{z}+\overline{u}$; d) Vertical flux of action F^z (contour) and action flux vector (F^x,F^z). In 1b) and 1d) the negative values are dashed. 22

Fig. 2. Surface pressure drag predicted by theory and normalized by the amplitude of the inviscid linear mountain gravity wave drag produced by a mountain of height H in a uniform flow of intensity $U = u_0\left(\frac{\delta(L^{-1})}{2}\right)$ and of stratification N: UNH^2 (in non dimensional form: $\frac{\overline{\delta}(1)}{2}\sqrt{(J)}S^2$, see Eq. 22). Grey dots are from the MITgcm with $S = 0.15$. 23

Fig. 3. a) Vertical profiles of the normalized wave Reynolds stress, $\overline{\overline{u}\,\overline{w}}$, for $S = 0.01$. b) Pressure (black solid) and viscous (black dashed) stresses as defined on the RHS of Eq. (23). 24

Fig. 4. a) Normalized Reynolds stress emitted in the far field $\overline{\overline{u}\overline{w}}(\infty)$; b) Minimum value of $\overline{\overline{u}\,\overline{w}}(z)$ for $0 < \overline{z} < \infty$. Grey dots are from the MITgcm with $S = 0.15$. 25

Fig. 5. Same as Fig. 1 for $S = 0.15$. 26

Fig. 6. Vertical velocity for different values of the Richardson number J and of the slope S. Boundary layer depth $\delta(1) = 0.1$. Contour intervals are shown in each panels. 27

Fig. 7. Wind vectors around the hill and for different values of the Richardson number J and of the slope S. Boundary layer depth $\delta(1) = 0.1$. 28

Fig. 8. Upstream blocking versus downslope windstorm index defined as the ratio between the max downslope wind amplitude and the max upslope wind amplitude. Grey dots are from the MITgcm with $S = 0.15$. 29

Fig. 9. Vertical velocities from the MITgcm in the upper panels correspond to the theory in Figs. 6d),6e) and 6f). Wind vectors from the MITgcm in the lower panels correspond to the theory in Figs. 7d),7e) and 7f). 30

Fig. 10. Uniform solutions used to invert boundary conditions and to evaluate the wave fields over the entire domain. $J = 1$, $\mathrm{Pr} = 0.5$. All the solutions are expressed using inner variables. . . 31

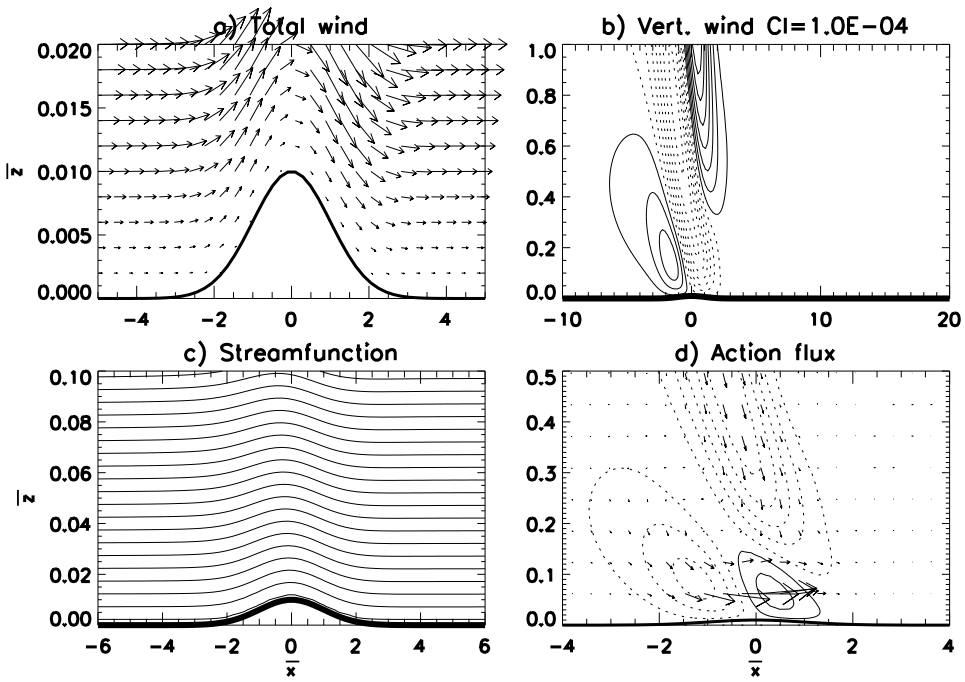

FIG. 1. Physical fields predicted by the theory in the hydrostatic case and when $J = 4$, $S = 0.01$, $\overline{\delta} = 0.1$. a) Total wind vector $(\overline{z}+\overline{u},\overline{w})$, b) vertical wind $\overline{w}$; c) total stream function $\overline{\psi}$ defined by: $\partial_{\overline{z}}\overline{\psi} = \overline{z}+\overline{u}$; d) Vertical flux of action F^z (contour) and action flux vector (F^x, F^z). In 1b) and 1d) the negative values are dashed.

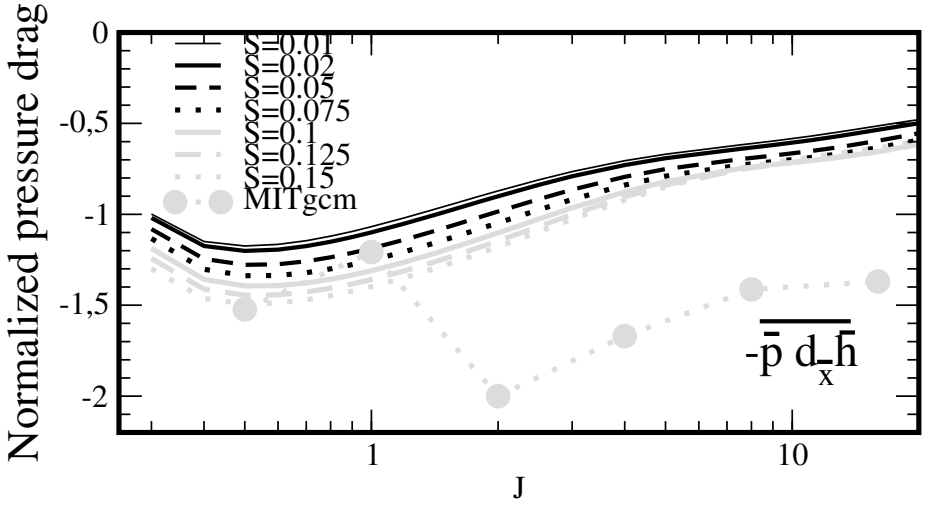

619 FIG. 2. Surface pressure drag predicted by theory and normalized by the amplitude of the inviscid linear
620 mountain gravity wave drag produced by a mountain of height H in a uniform flow of intensity $U = u_0\left(\frac{\delta(L^{-1})}{2}\right)$
621 and of stratification N: UNH^2 (in non dimensional form: $\frac{\overline{\delta}(1)}{2}\sqrt{(}J)S^2$, see Eq. 22). Grey dots are from the
622 MITgcm with $S = 0.15$.

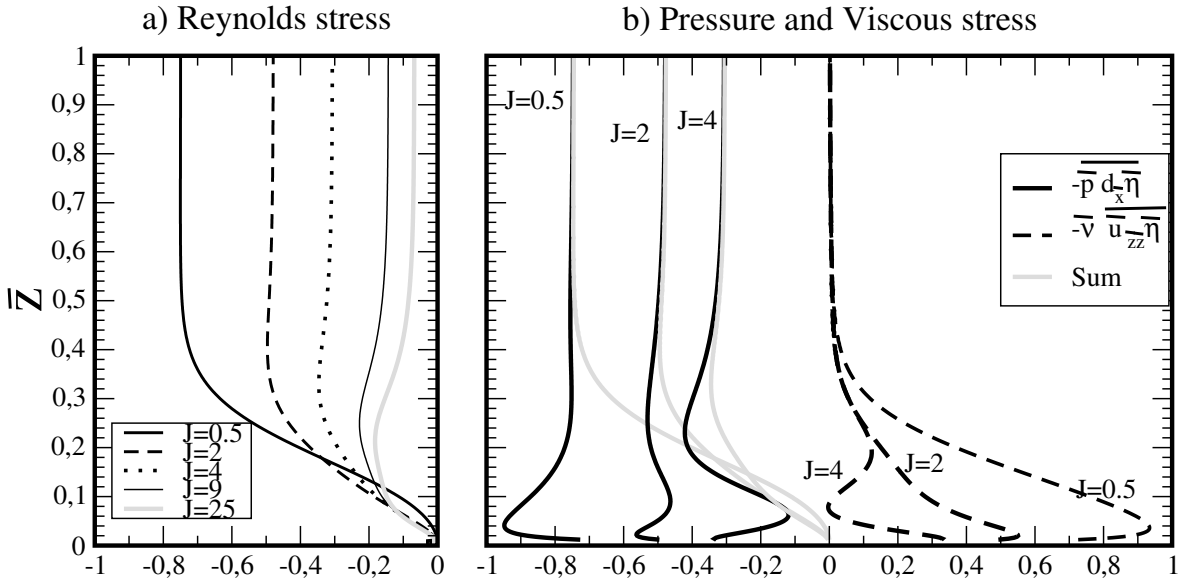

623 FIG. 3. a) Vertical profiles of the normalized wave Reynolds stress, $\overline{\overline{u}\,\overline{w}}$, for $S = 0.01$. b) Pressure (black
624 solid) and viscous (black dashed) stresses as defined on the RHS of Eq. (23).

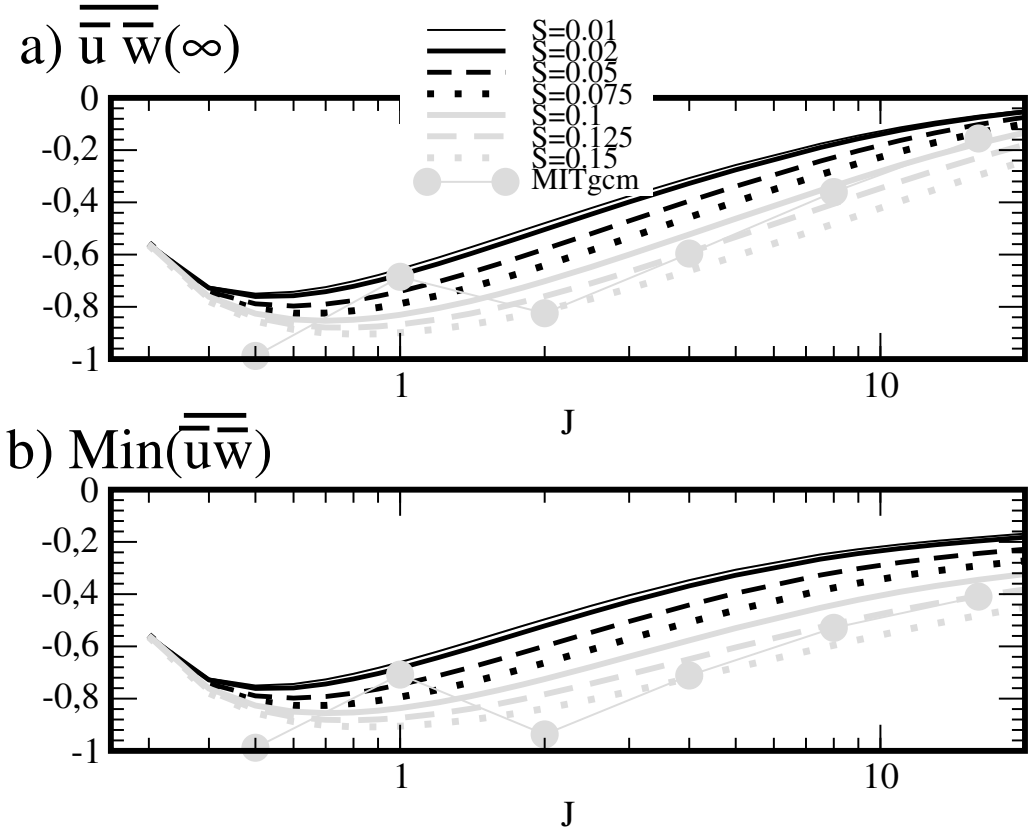

625 FIG. 4. a) Normalized Reynolds stress emitted in the far field $\overline{\overline{uw}}(\infty)$; b) Minimum value of $\overline{\overline{u}\,\overline{w}}(z)$ for
626 $0 < \overline{z} < \infty$. Grey dots are from the MITgcm with $S = 0.15$.

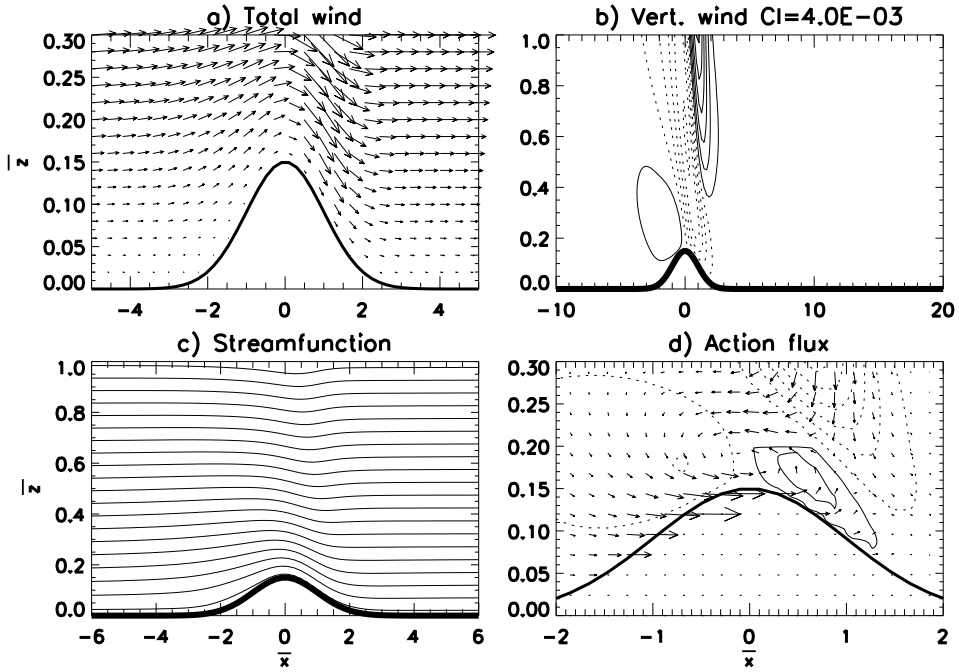

FIG. 5. Same as Fig. 1 for $S = 0.15$.

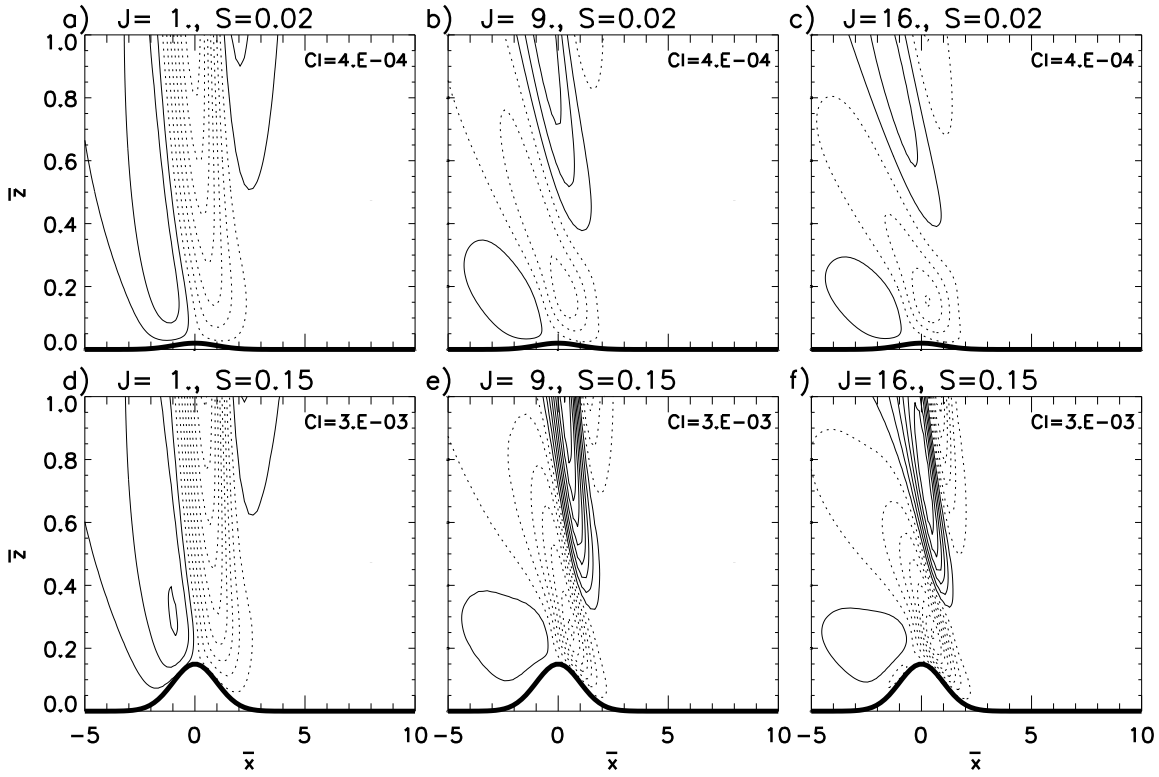

627 FIG. 6. Vertical velocity for different values of the Richardson number J and of the slope S. Boundary layer
628 depth $\delta(1) = 0.1$. Contour intervals are shown in each panels.

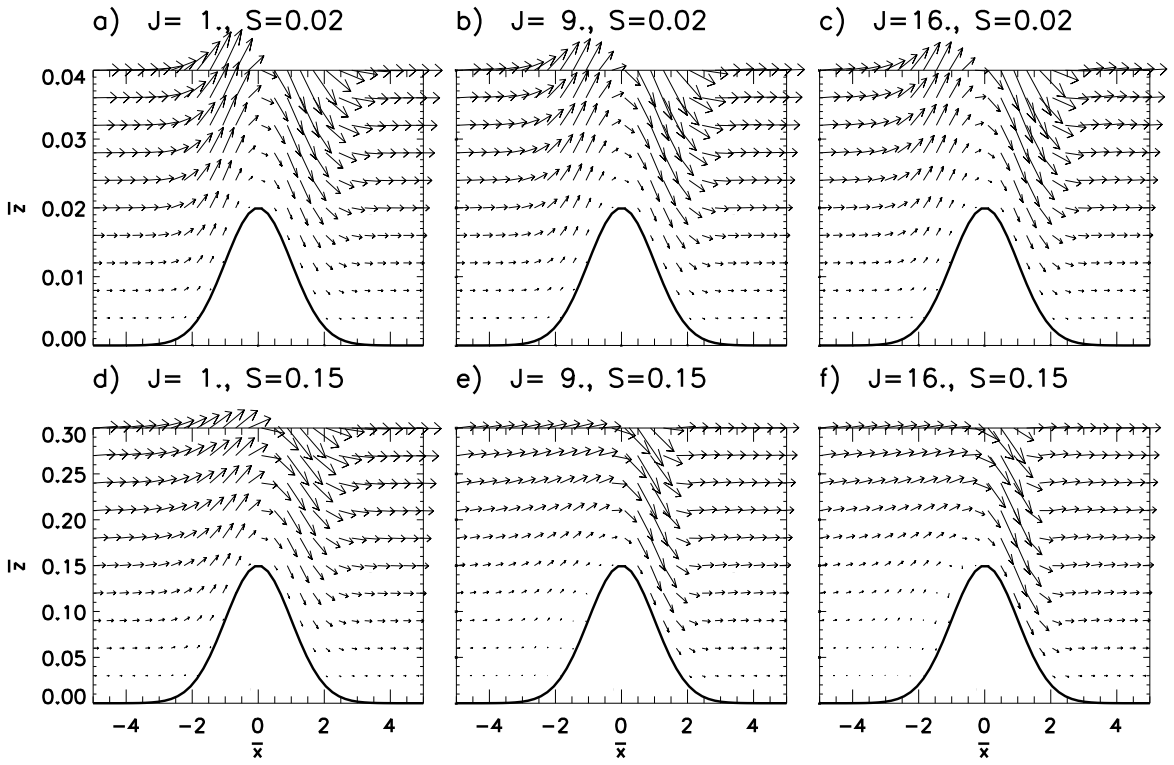

629 FIG. 7. Wind vectors around the hill and for different values of the Richardson number J and of the slope S.

630 Boundary layer depth $\delta(1) = 0.1$.

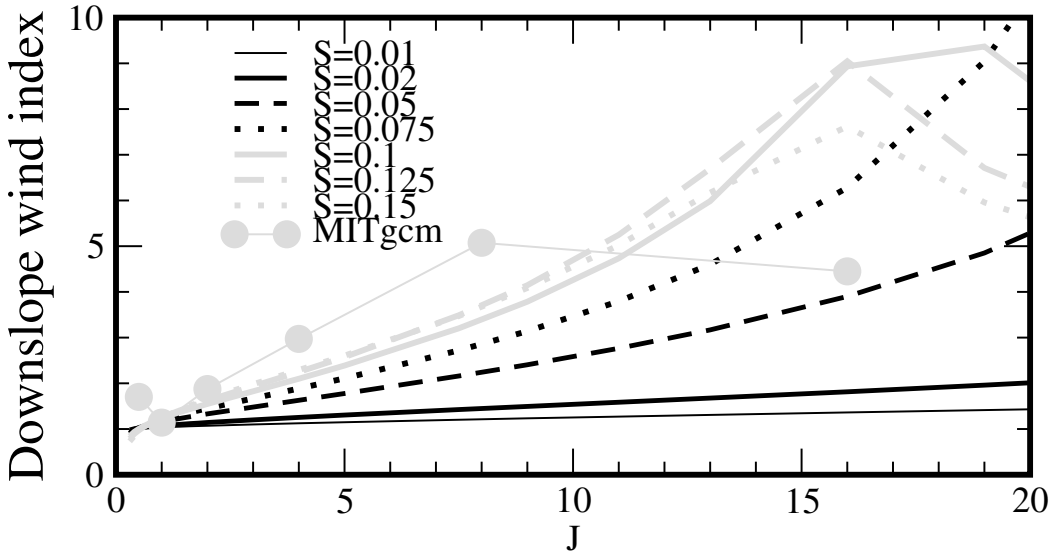

631 FIG. 8. Upstream blocking versus downslope windstorm index defined as the ratio between the max downs-
632 lope wind amplitude and the max upslope wind amplitude. Grey dots are from the MITgcm with $S = 0.15$.

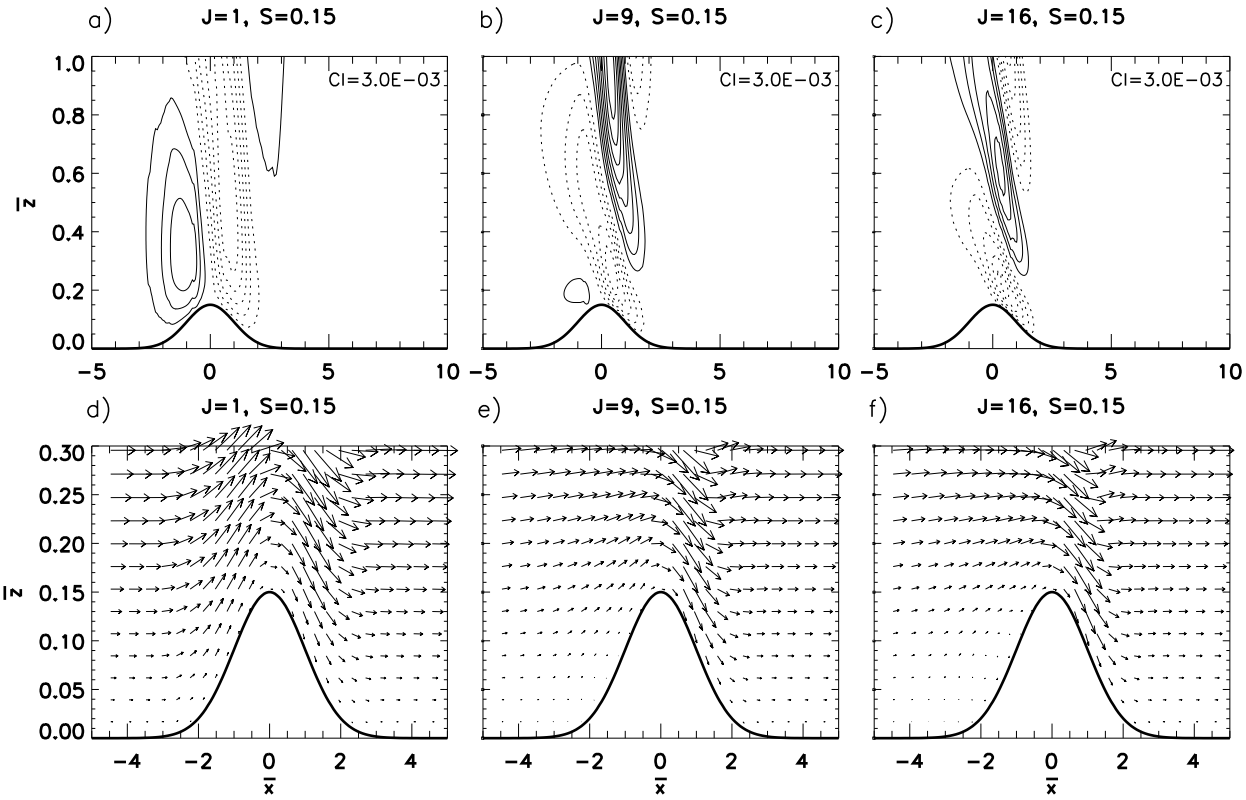

633 FIG. 9. Vertical velocities from the MITgcm in the upper panels correspond to the theory in Figs. 6d),6e) and
634 6f). Wind vectors from the MITgcm in the lower panels correspond to the theory in Figs. 7d),7e) and 7f).

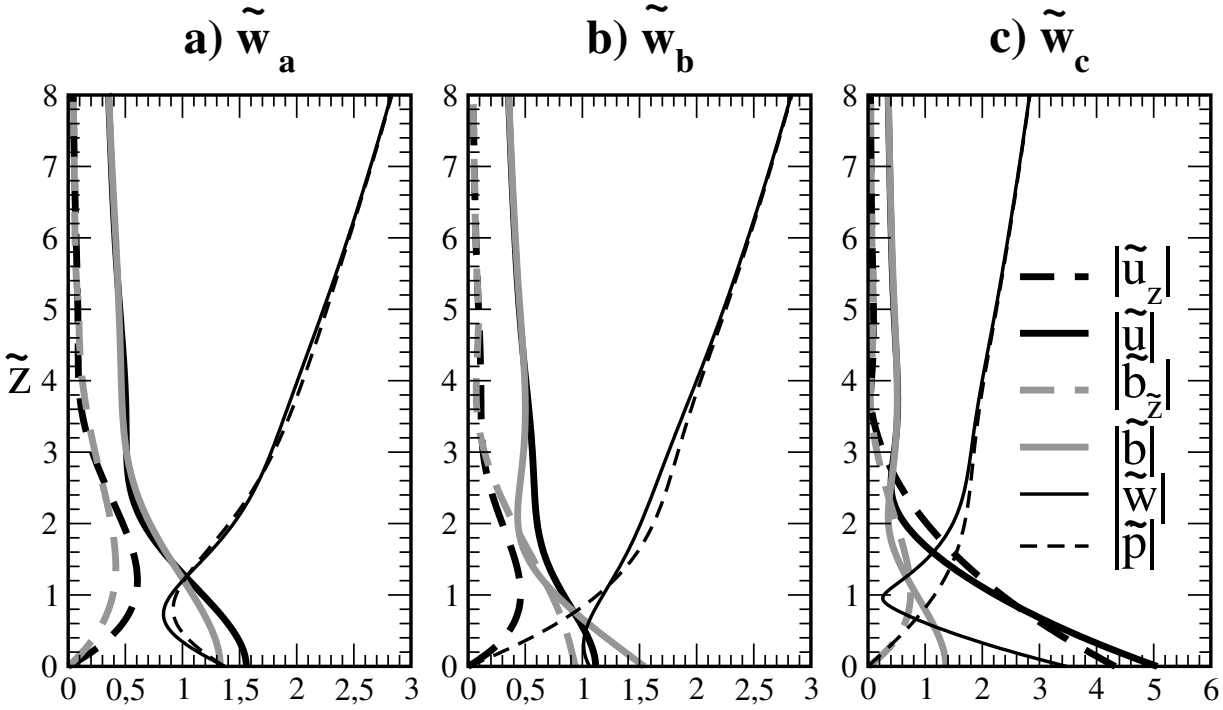

FIG. 10. Uniform solutions used to invert boundary conditions and to evaluate the wave fields over the entire domain. $J = 1$, $\mathrm{Pr} = 0.5$. All the solutions are expressed using inner variables.